


**Physical properties of monolayer Mn(BiTeS)<sub>2</sub> and its applications in sub-3 nm spintronic devices**Zhanhai Li, Jianing Han, Shengguo Cao, Zhenhua Zhang<sup>✉,\*</sup> and Xiaoqing Deng<sup>†</sup>*Human Provincial Key Laboratory of Flexible Electronic Materials Genome Engineering, Changsha University of Science and Technology, Changsha 410114, China* (Received 1 August 2023; revised 7 October 2023; accepted 3 November 2023; published 16 November 2023)

Half semiconductors, capable of achieving 100% spin-polarized carriers under simple electrostatic gating, optical excitation, and thermal excitation conditions, have emerged as some of the most promising materials for spintronics. Thus, to find new half-semiconducting materials is highly desirable. Herein, we propose a two-dimensional half-semiconducting material, Mn(BiTeS)<sub>2</sub>, and its various physical properties and potential applications are predicted. The energetic, dynamic, thermal, and mechanic stability is highly identified by variously related calculations, implying that Mn(BiTeS)<sub>2</sub> possibly exists in experiment. It holds a high magnetic anisotropy energy in the ferromagnetic ground state, with Curie temperature up to 54.3 K. It also possesses outstanding mechanical and optical properties as well as high carrier mobility. Besides, multiple kinds of sub-3 nm functional device prototypes are designed and their excellent transport behaviors are revealed. For example, the *pn*-junction diode exhibits a high spin filtering and strong rectification effect. While rectification for *A*-type *pin*-junction field-effect transistor is more advantageous, with rectification ratio reaching 10<sup>11</sup>. Besides, the *nin*-junction and *pip*-junction field-effect transistors manifest an intriguing negative differential resistance phenomenon. The *pip*-junction field-effect transistor can achieve 100% spin filtering, and the *pin*-junction phototransistor exhibits excellent optical response and can distinguish colors based on the spin-dependent photocurrents.

DOI: [10.1103/PhysRevB.108.184413](https://doi.org/10.1103/PhysRevB.108.184413)**I. INTRODUCTION**

With the rapid development of information technology, the demands on integration density, processing speed, and power consumption for electronic devices are becoming more and more stringent, pushing traditional silicon-based devices to a physical limit. To further enhance their performances, the research attention is turning into another intrinsic characteristic of electrons: spin. Its inclusion has provided a vast prospect to design new spintronic devices [1], which possess remarkable advantages such as low power consumption and nonvolatility compared to conventional electronic devices. Thus, it is of great significance to facilitate the development of computing technology and nonvolatile storage [2]. Due to the ability for magnetic semiconductors to manipulate both the charge and spin degrees of freedom of electrons [3,4], they are considered as one of the ideal solutions for the postsilicon electronic devices in the semiconductor technology revolution [5–7]. To expedite the development of these new electronic devices, efforts to investigate computational methods and novel magnetic materials have been intensified [8–11]. Particularly in recent years, huge breakthroughs have been achieved in the experiments; new two-dimensional (2D) magnetic materials such as Cr<sub>2</sub>Ge<sub>2</sub>Te<sub>6</sub> [12], CrI<sub>3</sub> [13], Fe<sub>3</sub>GeTe<sub>2</sub> [14], VSe<sub>2</sub> [15], and MnBi<sub>2</sub>Te<sub>4</sub> (MBT) [16] have been fabricated.

Recently, 2D MBT has been successfully synthesized and confirmed to be an intrinsic magnetic topological insulator

[16–19]. Due to the unique property of monolayered ferromagnetism and interlayered antiferromagnetism in multilayer MBT, it has also been demonstrated as an antiferromagnetic topological insulator [17–22]. As a multifunctional magnetic material, it exhibits various characteristics such as a tunable dynamical axion field, magnetic axion insulator, and the quantum anomalous Hall effect [23–26]. It shows also excellent spin transport property [27]. The design of magnetic tunnel junctions based on MBT|h – BN|MBT and Cu|n – layer – MBT|Cu (*n* = 1, 2, 3, 4) achieved a tunneling magnetoresistance ratio as high as 4 × 10<sup>3</sup>%, offering possibility to overcome the leakage current bottleneck in magnetic tunnel junctions [28,29]. Furthermore, a high spin polarization and perfect ohmic contact at the graphene-MBT-graphene interface have been realized, revealing its potential applications in future carbon circuits [30]. The unique magnetic and topological properties of MBT have accelerated the active exploration on its family members; for example, the bilayer and trilayer van der Waals antiferromagnetic Janus-MnBi<sub>2</sub>Se(S)<sub>2</sub>Te<sub>2</sub> based on MBT structure not only exhibit various antiferromagnetic topological magnetism, but also allow the control of this property by the relative positions of the two separated vertical monolayers [31]. Besides, a topological phase transition for the monolayered Janus-MnBi<sub>2</sub>Se(S)<sub>2</sub>Te<sub>2</sub> can be induced by an electric field, leading to a significant increase in magnetic anisotropy and Curie temperature with increasing electric field [32].

However, the studies on the MBT family are currently very limited. To expand MBT family and find new physics and promising applications in devices, in this present work, we propose a 2D material, monolayered

\*Corresponding author: zhzhang@csust.edu.cn

†Corresponding author: xq\_deng@163.com

Mn(BiTeS)<sub>2</sub> (ML-MBTS), with atomic-layer sequence S-Bi-Te-Mn-Te-Bi-S, which is different from the already-studied Janus-MnBi<sub>2</sub>Se(S)<sub>2</sub>Te<sub>2</sub> atomic structure, with Se(S)-Bi-Se(S)-Mn-Te-Bi-Te atomic-layer sequence [31], and its structural stability as well as magnetoelectronic, mechanical, optical, and spin transport properties are predicted and analyzed thoroughly. It is found that ML-MBTS is a half semiconductor in the ferromagnetic (FM) ground state, stemming from Goodenough-Kanamori-Anderson (GKA) superexchange magnetic interaction, and holds a high magnetic anisotropy energy, with Curie temperature up to 54.3 K. It also possesses outstanding mechanical and optical properties as well as high carrier mobility. Furthermore, we design multiple kinds of sub-3 nm functional device prototypes such as diode based on *pn* junction and field-effect transistors based on *pin* junction, *pip* junction, and *nin* junction, and their excellent transport behaviors are revealed, including high spin filtering and rectification effect, intriguing NDR phenomenon, excellent optical response, and distinguishing colors upon the magnitude of spin-up and spin-down photocurrents, and so on.

## II. METHODS

All calculations are performed by using QUANTUMATK [33] software package based on density-functional theory (DFT) combined with nonequilibrium Green's function method. The exchange-correlation potential is described by the spin-polarized generalized gradient approximation (SGGA) with the Perdew-Burke-Ernzerhof functional [34]. To account for the strong correlation effects in the localized *3d* electrons for Mn atoms, the SGGA+*U* method [35] is employed with  $U = 4.0$  eV [32]. To compare the results, the revised Heyd-Scuseria-Ernzerhof range-separated hybrid functional (HSE06) [36] is also used to calculate the band structure. The valence-electron wave functions are expanded by using the linear combination of atomic orbitals approach. The SG15 pseudopotential is used to describe the interaction between the valence electrons and atomic cores. To take into account interface effects appropriately, the interface dipole correction and Grimme's DFT-D3 method dispersion correction is included for multilayered MBTS. The real-space density-grid cutoff is set to 220 Hartree. For the structural optimization, the energy convergence threshold and the maximum Herman-Feynman force on a single atom are set to  $10^{-5}$  eV and  $10^{-2}$ , eV/Å, respectively. A vacuum layer of 2.0 nm is included to avoid interactions between model and its "image". The Brillouin-zone sampling grid for the unit cell and devices are set to  $27 \times 27 \times 1$  and  $9 \times 1 \times 150$ , respectively. For convenience, the Fermi level is set to 0.0 eV for all systems.

## III. RESULTS AND DISCUSSION

### A. Structural stability and basic physical properties of MBTS

#### 1. Structure stability

To obtain the ML-MBTS structure, we directly substitute the upper and lower Te atom layers in the monolayer MBT (Te-Bi-Te-Mn-Te-Bi-Te) with S atoms. Therefore, MBTS possesses the same space group as MBT ( $R\bar{3}m$ ), consisting of seven atomic layers (S-Bi-Te-Mn-Te-Bi-S) along the [0001]

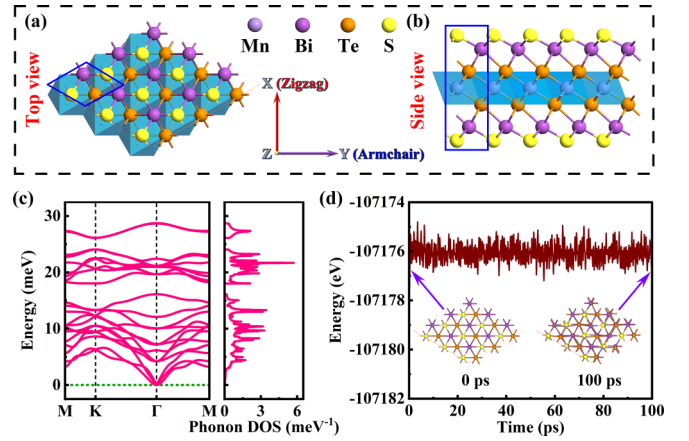


FIG. 1. ML-MBTS crystal structure: (a) top view, (b) side view, where region enclosed by blue frame represents ML-MBTS unit cell. (c) Phonon spectrum, and (d) molecular dynamics simulation result.

direction, with an *ABC* stacking sequence and an inversion symmetry with the Mn atom as the inversion center, as shown in Figs. 1(a) and 1(b), where the region enclosed by the blue frame represents the ML-MBTS unit cell, and the zigzag and armchair directions based on atomic hexagon configuration in ML-MBTS geometry are denoted as *X*- and *Y* axis, respectively. As we know, only highly stable two-dimensional materials are possible to be fabricated experimentally. Therefore, we make various assessments on stability of ML-MBTS. To evaluate the energy stability of ML-MBTS, we calculate its cohesive energy, defined as

$$E_{\text{coh}} = [E_{\text{MBTS}} - E_{\text{Mn}} - (E_{\text{Bi}} + E_{\text{Te}} + E_{\text{S}}) \times 2]/n, \quad (1)$$

where  $E_{\text{MBTS}}$  represents the total energy of the MBTS unit cell, while  $E_{\text{Mn}}$ ,  $E_{\text{Bi}}$ ,  $E_{\text{Te}}$ , and  $E_{\text{S}}$  are the energy for isolated atoms Mn, Bi, Te, and S, respectively.  $n$  corresponds to the total number of atoms in the unit cell, taking  $n = 7$  for our case. Using Eq. (1), we obtain the cohesive energy  $E_{\text{coh}} = -3.18$  eV/atom for ML-MBTS. The negative cohesive energy indicates that ML-MBTS is energetically stable. Furthermore, to estimate the dynamical stability of ML-MBTS, we calculate the phonon spectrum, as shown in Fig. 1(c). Clearly, the phonon spectrum of ML-MBTS consists of 3 acoustic branches and 18 optical branches. The in-plane transverse acoustic (TA) and longitudinal acoustic (LA) branches exhibit a linear dispersion near the  $\Gamma$  point, while the out-of-plane Z-directional acoustic (ZA) branch shows a quadratic dispersion. The absence of imaginary frequency throughout the whole Brillouin zone in the phonon spectrum confirms that ML-MBTS dynamical stability is high.

Figure 1(d) presents the molecular dynamics simulation of the  $3 \times 3$  MBTS supercell at room temperature in the *NVT* ensemble. The simulation employs the Nosé-Hoover method [37] for temperature control, with a thermal bath duration of 100 ps and a time step of 10 fs. During the simulation, the total energy fluctuates insignificantly, and all atom vibration only occurs near their equilibrium positions, maintaining the crystal structure well. After 100 ps of thermal bath simulation, the structure exhibits a slight deformation, but no bond break-

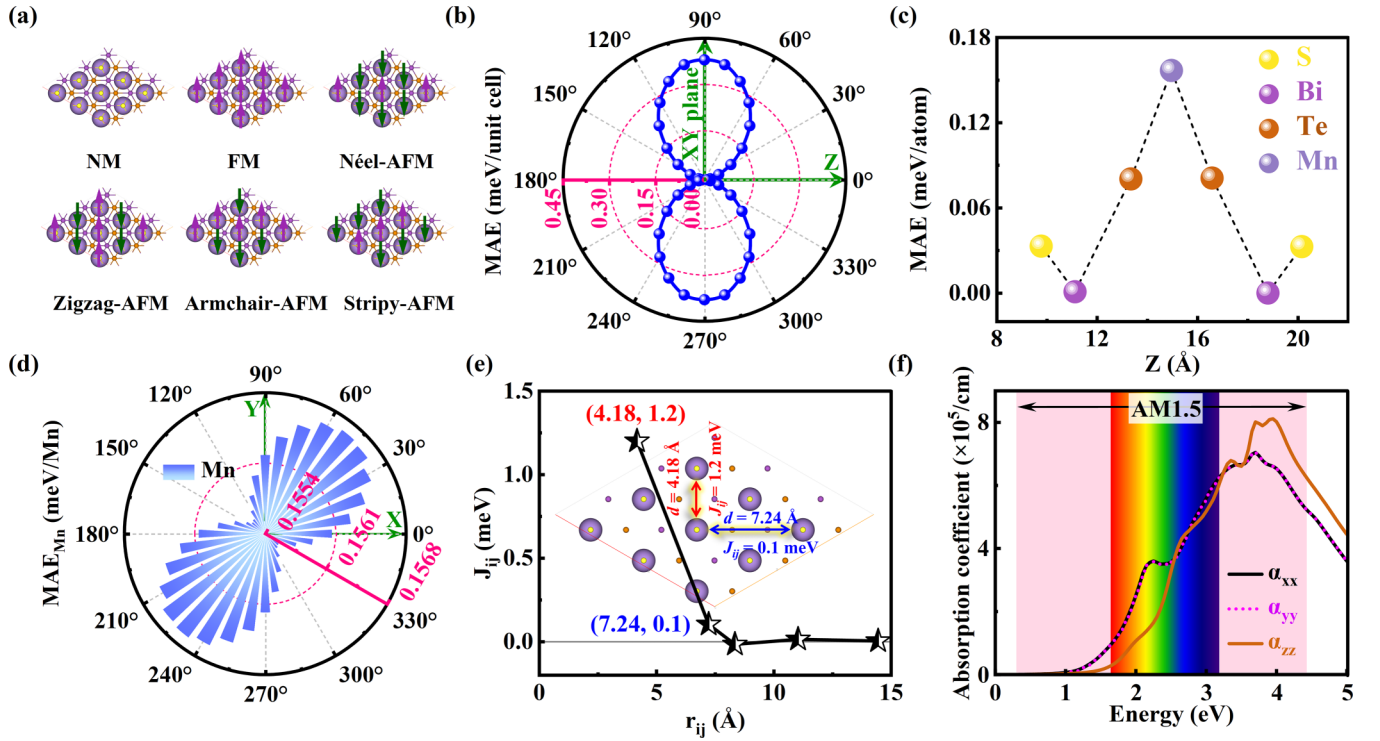


FIG. 2. ML-MBTS: (a) Various setting magnetic configurations, (b) magnetic anisotropy energy (MAE) in MBT unit cell vs polar angle  $\theta$  when taking  $\text{MAE} = E(\theta, 0) - E(0, 0)$ , where  $\theta$  represents angle between spin direction and Z axis, (c) contributions of individual atoms to total MAE in unit cell when taking  $\text{MAE} = E(\pi/2, 0) - E(0, 0)$ , (d) MAE of Mn atom vs azimuthal angle  $\Phi$  when taking  $\text{MAE} = E(\pi/2, \Phi) - E(0, 0)$ , where  $\Phi$  represents angle between projection of spin at XY plane and X-axis (zigzag) direction, (e) Heisenberg coupling coefficient  $J_{ij}$  vs distance between Mn atoms, and (f) optical absorption coefficient.

ing or structural reconstruction is observed. This demonstrates that ML-MBTS possesses a good thermodynamic stability and can stably exist at room temperature. Besides, we verify that the mechanical stability of ML-MBTS is also very high (see Sec. III A 5, *Mechanical property*, for details). In short, our various stability assessments have clearly identified that ML-MBTS is highly stable, indicating that its experimental fabrication might be highly feasible.

## 2. Magneto-electronic property

In suggesting ML-MBTS, each Mn atom bonds with six Te atoms to form an octahedral structure. The octahedral crystal field induces the Mn- $d$  orbital to be split into a higher-energy  $e_g$  state (based on  $d_z^2$  and  $d_{x^2-y^2}$  orbitals) and lower-energy  $t_{2g}$  state (based on  $d_{xy}$ ,  $d_{xz}$ , and  $d_{yz}$  orbitals). It is widely recognized that the orbital angular momentum and spin of 3d electrons in transition metal ions are the primary origins of magnetic moments in magnetic materials, and their interactions cause long-range magnetic ordering [13]. Based on the charge population analysis, the total magnetic moment of the ML-MBTS unit cell is  $5.006 \mu_B$ , with 99.98% weight for Mn atom, indicating that the magnetism in ML-MBTS is predominantly localized on the  $\text{Mn}^{2+}$  ( $3d^5$ ), with a spin  $S = 5/2$  for each  $\text{Mn}^{2+}$ , presenting a high-spin state. That is, each orbital of the doublet  $e_g$  and triplet  $t_{2g}$  is singly occupied by an electron with the entire same spin direction, leading to an incomplete filling. Additionally, the spin magnetic moments in one unit cell for various elements are listed in

Table S1 [38] of the Supplemental Material for clarity and comparison.

To find the magnetic ground state, we consider six possible magnetic couplings for ML-MBTS: nonmagnetic (NM), ferromagnetic (FM), Néel antiferromagnetic (AFM), zigzag AFM, armchair AFM, and stripy AFM, as displayed in Fig. 2(a). The computational results unequivocally identify the FM state serving as the magnetic ground state of ML-MBTS (see Fig. S1(a) [38]), which arises from the fact that all Mn-Te-Mn bond angles in the crystal are approximately  $90^\circ$ . According to the GKA rule [39–41], such bond angles facilitate a FM coupling between magnetic ions via nonmagnetic atoms as intermediaries; that is, the superexchange magnetic coupling occurs, thereby establishing the FM ground state for this material. The calculated lattice constant for ML-MBTS in the FM ground state is  $a = 4.18 \text{ \AA}$ .

Magnetic anisotropy is an important feature to judge the presence of long-range magnetic ordering in 2D materials. Here, we perform spin-orbit coupling calculations to investigate the magnetic anisotropy energy (MAE) as a function of spin orientation for ML-MBTS in the FM state. The MAE denotes the energy difference between two spin-polarization directions, and its angular dependence can be computed by

$$\text{MAE} = E(\theta, \Phi) - E(\theta_0, \Phi_0), \quad (2)$$

where  $\theta$  and  $\Phi$  are the polar and azimuthal angles, respectively, describing the spin-polarization direction. Here, we take  $E(\theta_0, \Phi_0) = E(0, 0)$  as the out-of-plane energy and  $E(\theta, \Phi) = E(\pi/2, \Phi)$  as the in-plane energy. Therefore, if

MAE =  $E(\pi/2, \Phi) - E(0, 0)$  is a positive (negative) value, then out-of-plane (in-plane) spin polarization occurs. Our calculated MAE for ML-MBTS is 0.38 meV per unit cell, indicating its pronounced out-of-plane spin polarization, that is, the Z axis (perpendicular to 2D plane) as the easy axis of magnetization [see Fig. 2(b)]. The presence of magnetic anisotropy can enhance the stability of magnetic ordering, thus providing resistance against thermal disturbance [12,42]. Figure 2(c) illustrates the contributions of each atom to total MAE. The primary contribution to the MAE originates from the Mn atoms, with the largest magnetic moments, followed by Te atoms, acting as mediators for superexchange interactions between Mn<sup>2+</sup> ions. Additionally, the surface S atoms also make a notable contribution, while the contribution of Bi atoms is negligible. To further investigate the relationship between the MAE and azimuthal angle  $\Phi$ , Fig. 2(d) exhibits the variation of MAE for the Mn atom as a function of  $\Phi$ . As can be seen, for the FM-coupled ML-MBTS, the least possible direction of spin polarization for the Mn atom layer is oriented along the direction  $(\theta, \Phi) = (\frac{\pi}{2}, \frac{(5+18n)\pi}{18})$  (where  $n$  is zero or an integer), and its magnetic anisotropy energy MAE<sub>out</sub> = 0.1567 meV/Mn.

In the following, we further discuss magnetic stability. As mentioned before, the magnetic moment in ML-MBTS primarily localizes on the Mn atoms. Therefore, the Heisenberg model can be employed to describe the exchange coupling between the localized spins, which is given by [43,44]

$$H = - \sum_{i \neq j} J_{ij} \hat{e}_i \cdot \hat{e}_j, \quad (3)$$

where  $J_{ij}$  represents the Heisenberg exchange-coupling constant, and  $\hat{e}_{ij}$  denotes the normalized local spin vectors on atoms  $i/j$ . Here, we define the exchange-coupling matrix element between atom  $i$  at the center cell labeled as 0 and atom  $j$  in a different cell with a lattice displacement vector  $\mathbf{R}$  as  $J_{i0, \mathbf{R}j}$ . Its value can be calculated by using the real-space Green function [44,45] derived from the original Liechtenstein-Katsnelson-Antropov-Gubanov formula [43], as expressed below:

$$J_{0i, \mathbf{R}j} = - \frac{1}{4\pi} \int_{-\infty}^{E_f} dE \text{ImTr}[\Delta_i G_{i,j}(E, \mathbf{R}) \Delta_j G_{i,j}(E, -\mathbf{R})], \quad (4)$$

where  $E_f$  represents the Fermi level of the system,  $G_{i,j}(E, \pm \mathbf{R})$  corresponds to the retarded Green function of electrons with energy  $E$  at lattice vectors  $\pm \mathbf{R}$ , and  $\Delta_{i/j} = H_{i/j}^{\uparrow} - H_{i/j}^{\downarrow}$  represents the difference between the upper and lower spin channels of the Hamiltonian matrix. The relationship between the  $J_{ij}$  values for Mn atoms and their interatomic distances is illustrated in Fig. 2(e). The nearest-neighbor Mn atoms have a distance of 4.18 Å, corresponding to a Heisenberg exchange-coupling constant of 1.2 meV. The next-nearest-neighbor Mn atoms with an interatomic distance of 7.24 Å have a Heisenberg exchange-coupling constant of 0.1 meV. The exchange-coupling constants for further neighbor Mn atoms and beyond them are smaller or zero. Based on these results, we estimate the Curie temperature ( $T_C$ ) of ML-MBTS

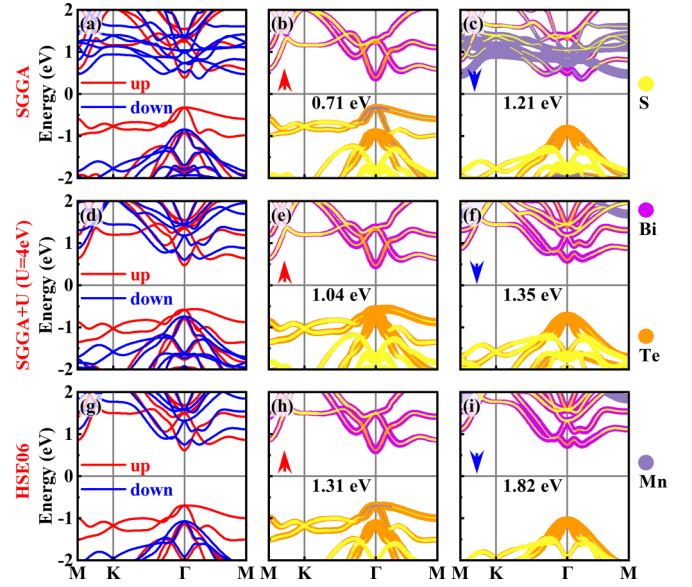


FIG. 3. Spin-resolved projected band structures obtained by using calculations of (a)–(c) SGGA, (d)–(f) SGGA+ $U$  ( $U = 4$  eV), and (g)–(i) HSE06, respectively.

by using the mean-field approximation (MFA) [44]:

$$T_C = \frac{2}{3k_B} \sum_{i0 \neq jR} J_{i0jR}, \quad (5)$$

where  $k_B$  represents the Boltzmann constant. The calculated Curie temperature for ML-MBTS is 54.3 K. It is higher than that for monolayer  $(\text{Bi}_{0.95}\text{Mn}_{0.05})_2\text{Te}_3$  (16 K) [46] and  $X$ -doped  $\text{Mn}_2\text{Bi}_2\text{Te}_5$  monolayers [ $X = \text{Sc}$  (26 K) and Mn (33 K)] [47], which were obtained by a similar calculation manner.

Figure 3 shows the ground-state (FM) band structure of ML-MBTS by using the SGGA, SGGA+ $U$  ( $U = 4$  eV), and HSE06 calculations, respectively. Clearly, there exists a difference in these band structures. With SGGA calculation, the band gap is underestimated, and the spin-up/spin-down band gaps are only 0.71 eV/1.21 eV, significantly smaller than those obtained from the other two methods. The conduction-band minimum (CBM) and valence-band maximum (VBM) are contributed by spin-down and spin-up states, respectively, located along the  $\Gamma$ - $M$  path and at the  $\Gamma$  point, indicating a bipolar magnetic semiconductor (BMS) property for ML-MBTS [see Figs. 3(a)–3(c)], but very close to half-semiconductor (HSC) [48] behavior. However, the CBM and VBM of ML-MBTS obtained from the SGGA+ $U$  and HSE06 calculations are both contributed by spin-up states, exhibiting a noticeable HSC property, with CBM and VBM located at the  $\Gamma$  point and along the  $\Gamma$ - $M$  path, respectively [see Figs. 3(d) and 3(g)]. In short, ML-MBTS is predicted to be BMS by SGGA calculation but it is possible to be HSC by SGGA+ $U$  and HSE06 calculations. Then, how to determine the most possible magnetic phase? Generally speaking, when the same prediction is obtained from two out of three calculation methods, one tends to think that such a prediction is the most likely one; thus, we believe that the most possible magnetic phase for ML-MBTS is HSC. More importantly, this

result can also be supported by additional theoretical studies such as investigations on ML-MBT. The previous SGGA+ $U$  ( $U = 4$  eV) calculations [19,27] and our SGGA+ $U$  ( $U = 4$  eV) and HSE06 calculation (see Figs. S2(f) and S2(g) [38]) all reveal that ML-MBT is HSC. As we know, ML-MBT and ML-MBTS are similar materials, belonging to the same material family; thus, the same theoretical method is applicable to make a reasonable prediction for properties of ML-MBTS, and we conclude that ML-MBTS should be HSC. However, it is worth mentioning that the SGGA+ $U$  method holds a lower computational cost compared to HSE06 calculation, making the SGGA+ $U$  method advantageous, particularly in a huge calculation task such as for device transport investigations. Thereby, in our following studies, we only adopt the SGGA+ $U$  method for all computations.

Now, we turn to make brief comparisons for the geometrical parameter and magnetoelectronic property between our studied ML-MBTS and already studied ML-MBT. The previous study displayed that the ML-MBT holds a lattice constant  $\alpha = 4.34$  Å [32], its MAE is 0.125 meV/Mn, with an out-of-plane easy magnetic axis [20], and the experimentally measured Curie temperature is 20 K [16], but no MFA theoretical calculated result for Curie temperature has been presented so far. Here, we also perform theoretical investigations on these physical quantities for the ML-MBT, as shown in Figs. S2(a)–S2(d) [38], where our obtained lattice constant for MBT (see Fig. S2(a) [38]) is  $\alpha = 4.34$  Å, entirely consistent with the previously reported value [32], but it is larger than that for our studied MBTS,  $\alpha = 4.18$  Å. Our obtained MAE for ML-MBT is 0.104 meV/Mn, with an out-of-plane easy magnetic axis, and Curie temperature is 30.2 K based on the MFA calculation (see Figs. S2(b) and S2(c) [38]). Clearly, our obtained MAE is slightly lower than the previous report [20], while our obtained Curie temperature overestimates the Curie temperature value to a certain degree compared with the experimental result [16]. Obviously, these values are lower than those for ML-MBTS, 0.1567 meV/Mn for MAE and 54.3 K for Curie temperature, as mentioned above, suggesting that ML-MBTS we construct is beneficial to enhance the magnetic stability compared with ML-MBT. Furthermore, based on Ref. [27] by using the SGGA+ $U$  calculation, ML-MBT is a HSC with a spin-up (spin-down) band gap of 1.1 (1.3) eV. We also calculate the band structure for ML-MBT by using SGGA, SGGA+ $U$  ( $U = 4$  eV), and HSE06 methods, as shown in Figs. S2(e) and S2(f) [38]. It is found that ML-MBT is a HSC with a spin-up (spin-down) band gap of 1.05 (1.24) eV upon SGGA+ $U$  calculation, essentially consistent with the previous study [27]. As presented above, our studied ML-MBTS is a HSC with a spin-up (spin-down) band gap of 1.04 (1.35) eV, thus holding a larger spin-down band gap than ML-MBT.

As stated above, to construct ML-MBTS, we directly substitute the upper and lower Te atom layers in the ML-MBT with S atoms. This is because S and Te atoms belong to the same main group and have a similar chemical property; thus, using S atoms to replace Te atoms generally does not cause a significantly geometrical deformation, favorably to the structural and magnetic stability. Of course, the properties of S and Te atoms also hold some differences such as electronegativity, which will lead to a distinct polarity between S-Bi and Te-Bi

covalent bonds, thus making different electrostatic potential and electronic states occur in materials, and giving rise to different physics for ML-MBTS. As shown in Fig. S3 [38], we can see that atomic orbital-projection density of states (DOS) have obvious differences for the same element when it is included in different materials (ML-MBTS and ML-MBT), implying that the S atom replacing Te atom effects in outer layer would induce the significant variations of electronic state for inner-layered Te atoms through the middle Bi atom layer. In particular,  $p_x$ - and  $p_y$ -orbital DOS in the valence band for inner-layered Te atoms is noticeably higher in ML-MBTS than that in ML-MBT, suggesting that a stronger orbital coupling and hybridization can be caused between inner-layered Te and Mn atoms in ML-MBTS. As mentioned before, the superexchange FM coupling occurs between Mn atoms via adjacent Te atoms as intermediaries. Therefore, the enhanced magnetic stability for ML-MBTS can be expected.

### 3. Magnetism of multilayered MBTS

In the following text, we briefly discuss the layer-dependent magnetic property of MBTS. Six different stacking configurations are considered, as illustrated in Fig. S4 [38], where the models aligning the lower S atom layer in the upper ML-MBTS with the nearest S atom layer, Bi atom layer, Te atom layer, S-Bi bridge site, Bi-Te bridge site, and Te-Mn bridge site in the lower ML-MBTS are denoted as S-S, S-Bi, S-Te, S-SBi, S-BiTe, and S-TeMn, respectively, for short. After sufficient relaxation, and with calculation on the total energy for each stacking model, the S-Bi stacking model is found to be the most energetically favorable (see Fig. S5 [38]). With an increase in the number of stacked layers, we observe that the multilayered MBTS exhibits an A-type AFM structure [49], similarly to the case of multilayered MBT [20], involving the FM coupling inside the layer but the AFM coupling between adjacent two layers, as shown in Figs. S1(b)–S1(f) [38]. However, the multilayered MBT is sensitive to the layer parity; when it holds an odd/even number of layers, the system exhibits/does not exhibit a residual magnetic moment due to the opposite spin polarization directions between adjacent layers, thereby showing sub-FM/AFM property. The even-layered system possesses combined time and spatial inversion symmetries [20]. While for the multilayered MBTS this is different, regardless of the number of stacked layers being odd or even, its band structure holds a spin splitting and exhibits sub-FM property. How to understand this behavior? As stated before, the magnetism in ML-MBTS generates from Anderson superexchange interaction [41] between adjacent Mn atoms, and the spin polarization in the Mn atom layer possesses a distribution probability in the range of azimuth angle around  $\Phi = (5 + 18n)\pi/18$  (where  $n$  is zero or an integer) [see Fig. 2(d)]. Just this fact leads to that the magnetic moment between two adjacent MBTS layers with AFM coupling might not be opposite completely, hereby there exists a finitely net magnetic moment in the multilayered MBTS system, even if it is an even-layered MBTS system. Such a net magnetic moment causes the spin splitting for band structure. The band-gap size remains around 1.0 eV with a slight fluctuation as the number of layers increases, and an indirect band gap feature is always preserved (see Fig. S6

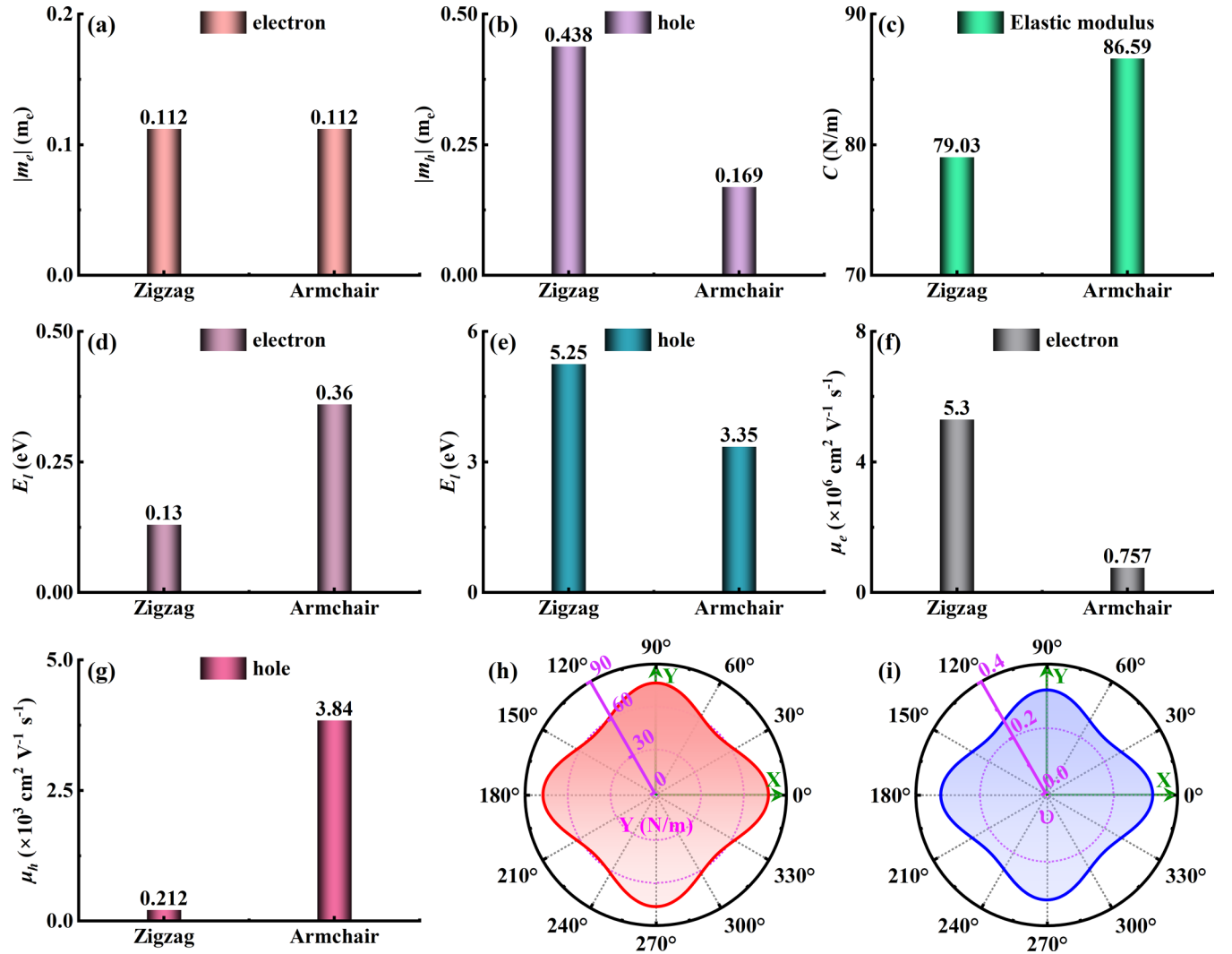


FIG. 4. (a) Effective mass of electrons, (b) effective mass of holes, (c) elastic modulus, (d) electron deformation potential constant, (e) hole deformation potential constant, (f) electron mobility, (g) hole mobility, (h) Young's modulus, and (i) Poisson's ratio.

[38]). In short, the versatile magnetic states of multilayered MBTS provide more possibilities for designing the magnetic tunneling junction devices.

#### 4. Carrier mobility

As we know, the suitable band gap and high carrier mobility are of extreme importance for the practical applications of materials in nanoelectronics and optoelectronics. Studies indicated that the mobility of semiconductor materials is primarily determined by electron-phonon scattering. Therefore, we employ the deformation potential theory (DPT) to estimate the mobility of ML-MBTS according to the following formula [50]:

$$\mu_{2D} = \frac{2e\hbar^3 C}{3k_B T |m^*|^2 E_1^2}, \quad (6)$$

where  $e$ ,  $\hbar$ ,  $k_B$ , and  $T$  represent the electronic charge, reduced Planck constant, Boltzmann constant, and temperature, respectively.  $m^*$  denotes the effective mass of electrons or holes, which is calculated by using  $m^* = \hbar^2(\partial^2 E(k)/\partial k^2)^{-1}$ .

Here,  $E(k)$  represents the energy dispersion relation in the vicinity of the band edges (CBM and VBM), and  $k$  is the wave vector.  $C$  is the tensile elastic modulus, which is computed as  $C = (\partial^2 E_{\text{total}}/\partial \varepsilon^2)/S$ , where  $E_{\text{total}}$  represents the total energy of one supercell,  $\varepsilon$  is the strain along the computational direction, and  $S$  is the area of the supercell.  $E_1$  is the deformation potential constant, defined as  $E_1 = \partial E_{\text{edge}}/\partial \varepsilon$ , where  $E_{\text{edge}}$  corresponds to the energy of the CBM and the VBM.

The calculated effective mass of carriers, tensile elastic modulus, and deformation potential constants for ML-MBTS are shown in Figs. 4(a)–4(e), and the related computation details can be found in Fig. S7 [38]. The obtained effective mass along the armchair (zigzag) direction is  $|m^*| = 0.112 m_e$  ( $0.112 m_e$ ) for electrons and  $|m^*| = 0.169 m_e$  ( $0.438 m_e$ ) for holes, respectively, as presented in Figs. 4(a) and 4(b), where  $m_e$  represents the bare electron mass. It is evident that the hole dispersion along the armchair direction is stronger compared to the zigzag direction, indicating favorable carrier transport along the armchair direction. The elastic constants  $C$  along the armchair (zigzag) direction are 86.59 (79.03) N/m [see Fig. 4(c)]. This suggests that there is a stiffer resistance to

applied strain in the armchair direction compared to the zigzag direction. In other words, after carrier-phonon scattering, the less energy is absorbed by phonon in the armchair direction, benefiting carrier transport. The deformation potential constants for electrons along the armchair (zigzag) direction are  $|E_1| = 0.36$  (0.13) eV, while for holes,  $|E_1| = 3.35$  (5.25) eV [see Figs. 4(d) and 4(e)]. A smaller deformation potential constant implies that carriers undergo minimal energy changes after scattering by phonon, which favors carrier transport.

Based on the above-obtained  $|m^*|$ ,  $C$ , and  $|E_1|$ , as well as using Eq. (6), the carrier mobility of ML-MBTS at room temperature ( $T = 300$  K) is achieved, as shown in Figs. 4(f) and 4(g). It is evident that the mobility along the armchair (zigzag) direction is  $\mu_e = 7.57 \times 10^5$  ( $5.30 \times 10^6$ )  $\text{cm}^2 \text{V}^{-1} \text{s}^{-1}$  for electrons and  $\mu_h = 3.84 \times 10^3$  ( $2.12 \times 10^2$ )  $\text{cm}^2 \text{V}^{-1} \text{s}^{-1}$  for holes. These values significantly surpass the mobility of monolayer  $\text{MoS}_2$ , 72.16 (60.32)  $\text{cm}^2 \text{V}^{-1} \text{s}^{-1}$  for electrons and 200.52 (152.18)  $\text{cm}^2 \text{V}^{-1} \text{s}^{-1}$  for holes along the armchair (zigzag) direction [51], and are comparable to the electron mobility of silicene and graphene,  $2.57 \times 10^5$  ( $2.58 \times 10^5$ ) and  $3.20 \times 10^5$  ( $3.39 \times 10^5$ )  $\text{cm}^2 \text{V}^{-1} \text{s}^{-1}$  along the armchair (zigzag) direction, respectively [52]. They are all obtained by DPT calculation. High carrier mobility implies that carriers in materials move easily under applied external electric field, which is a prerequisite for achieving high-performance and low-power nanoelectronic devices.

### 5. Mechanical property

To predict the mechanical property of ML-MBTS, its four independent elastic constants are calculated,  $C_{11} = 86.25$  N/m,  $C_{22} = 85.5$  N/m,  $C_{12} = 27.55$  N/m, and  $C_{66} = 29.05$  N/m. It is evident that ML-MBTS satisfies the Born-Huang stability criteria [53]:  $C_{11} > |C_{12}|$ ,  $\eta = C_{11}C_{22} - C_{12}^2 > 0$ , and  $C_{66} > 0$ , indicating that it holds a high mechanical stability. Based on the elastic constants, the Young modulus  $Y(\theta)$  and Poisson ratio  $\nu(\theta)$  as a function of the in-plane angle  $\theta$  can be calculated by [54]

$$Y(\theta) = \frac{\eta}{C_{11}\sin^4\theta + \chi\sin^2\theta\cos^2\theta + C_{22}\cos^4\theta} \quad (7)$$

$$\nu(\theta) = \frac{C_{12}\sin^4\theta - \zeta\sin^2\theta\cos^2\theta + C_{12}\cos^4\theta}{C_{11}\sin^4\theta + \chi\sin^2\theta\cos^2\theta + C_{22}\cos^4\theta}, \quad (8)$$

where  $\chi = \eta/C_{66} - 2C_{12}$  and  $\zeta = C_{11} + C_{22} - \eta/C_{66}$ . The computed results for  $Y(\theta)$  and  $\nu(\theta)$  are shown in Figs. 4(h) and 4(i), respectively. Young's modulus exhibits an in-plane anisotropy, reaching maximum and minimum values of 77.37 and 58.21 N/m at  $\theta = n\pi/2$  and  $(2n+1)\pi/4$ , respectively, which are comparable to Janus  $\text{GeSSe}$  (70.65 N/m) [55] and Si (60.6 N/m) [53]. Poisson's ratio shows a similar trend to Young's modulus, with maximum and minimum values, 0.32 and 0.24, also occurring at  $\theta = n\pi/2$  and  $(2n+1)\pi/4$  (where  $n$  is zero or an integer), respectively. In comparison to graphene, with high Young's modulus (342.2 N/m) and isotropic Poisson's ratio [53], relatively lower Young's modulus and anisotropic Poisson's ratio for ML-MBTS suggest its potential applications in flexible nanoelectronic strain sensors.

### 6. Optical property

To characterize the material's behavior under optical radiation and its light absorption intensity at specific wavelengths, we computed the optical absorption coefficient of ML-MBTS by using the following formula [56]:

$$\alpha(\omega) = \sqrt{2}\omega \left[ \sqrt{\varepsilon_1^2(\omega) + \varepsilon_2^2(\omega)} - \varepsilon_1(\omega) \right]^{1/2}, \quad (9)$$

where  $\varepsilon_1(\omega)$  and  $\varepsilon_2(\omega)$  represent the real and imaginary parts of the complex dielectric function, respectively. The calculated results are shown in Fig. 2(f), revealing that the optical absorption coefficient of ML-MBTS is isotropic in the in-plane directions, i.e.,  $a_{xx} = a_{yy}$ . The out-of-plane absorption coefficient ( $a_{zz}$ ) is higher than the in-plane counterpart. Both absorption peaks occur in the ultraviolet region, with magnitudes reaching  $10^5$ . Due to the higher density of states close to the Fermi level for the spin-up state, leading to that the spin-up state makes more contributions to the optical absorption. The high absorption characteristics in the ultraviolet range make ML-MBTS a promising candidate for ultraviolet photodetectors [57]. Furthermore, a broad absorption peak is observed within the AM1.5 standard solar spectrum energy range (0.3 ~ 4.43 eV), suggesting its potential in developing photovoltaic devices within the AM1.5 standard [58].

### B. Applications of ML-MBTS in sub-3 nm spintronic devices

As discussed above, ML-MBTS exhibits exceptional structural stability, excellent magnetoelectronic, mechanical, and optical properties, as well as high carrier mobility. These characteristics promise great potential for developing high-performance electronic devices based on ML-MBTS. In the following, we will focus our investigations on ML-MBTS-based sub-3 nm  $pn$ -junction diodes, sub-3 nm field-effect transistors, and optoelectronic transistors, including their model designs, transport characteristics, and underlying physical mechanisms.

#### 1. Sub-3 nm diode

The sub-3 nm  $pn$ -junction diode model based on ML-MBTS is illustrated in Fig. 5(a), where the transport direction is set along its armchair orientation, referred to as the A-type diode. Such a device consists of three parts: a source, a drain, and a central scattering region. The  $p$ -type and  $n$ -type doping are performed to the left area (source electrode+left scattering region) and right area (drain electrode+right scattering region) in the device, respectively, with doping concentrations of  $6 \times 10^{13} \text{cm}^{-2}$ , equivalently to a moderate bulk doping concentration of  $10^{20} \text{cm}^{-3}$ . Consequently, a  $pn$  junction is formed in the middle of the central scattering region in the device. The doping method employed here is the atomic charge compensation method [59], which is widely used in modeling nanoelectronic devices due to its complete independence of the system size and structure; particularly, it does not depend on the exact atomic position details of the doped impurities. To investigate the spin polarization and rectification effect of this  $pn$ -junction diode, the spin-dependent current is calcu-

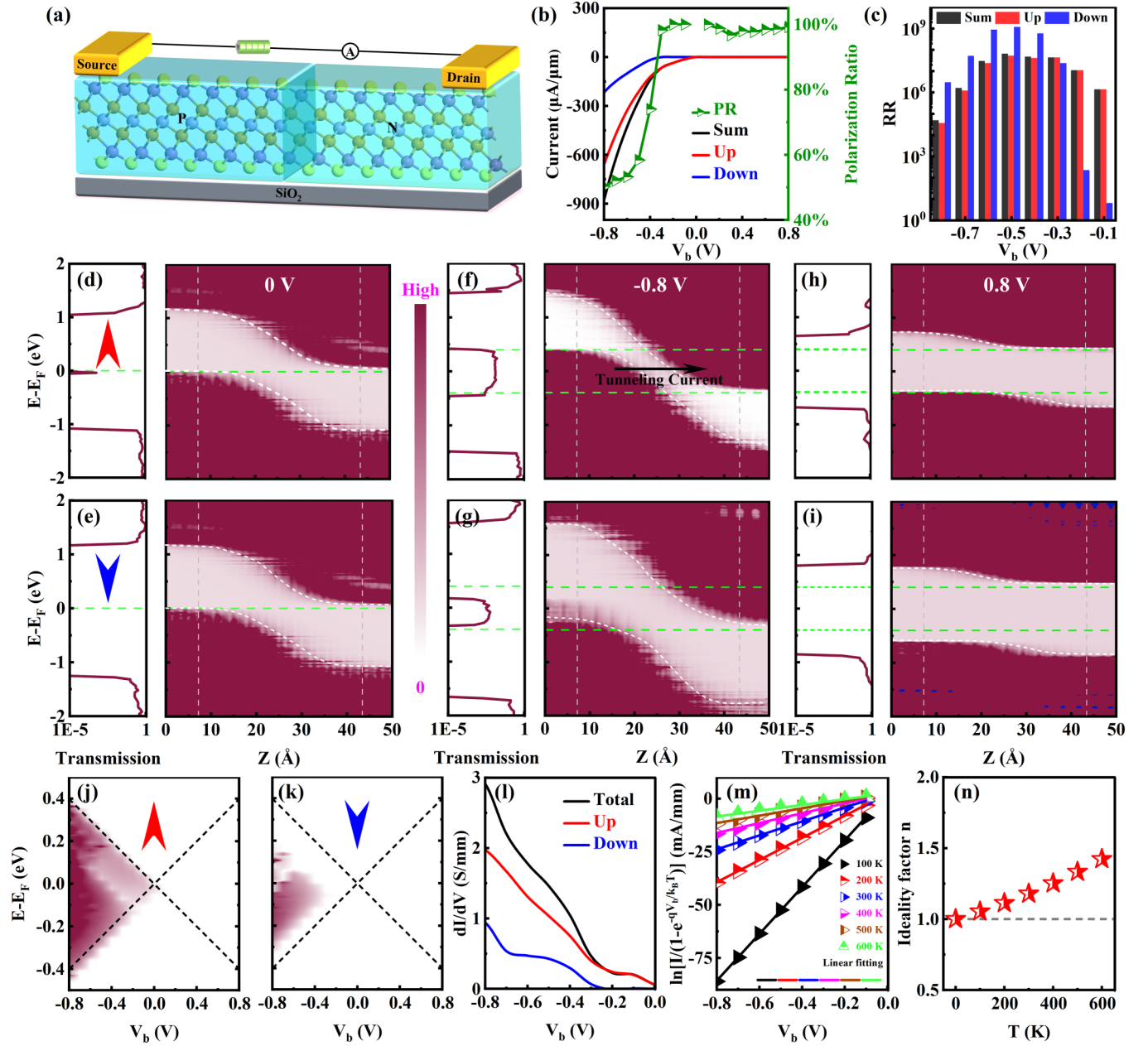


FIG. 5. A-type *pn*-junction diode: (a) Schematic diagram, (b) *I*-*V* curve, and (c) rectification ratio. Transmittance spectra (left) and PLDOS (right) for spin-up/spin-down states: (d), (e)  $V_b = 0$  V; (f), (g)  $V_b = -0.8$  V; and (h), (i)  $V_b = 0.8$  V. Bias-dependent transmittance spectra for (j) spin-up state and (k) spin-down state. (l) Differential conductance density ( $dI/dV$ ) curve. (m)  $\ln[I/(1 - e^{-qV_b/k_B T})]$  as function of bias voltage. (n) Ideality factor as function of temperature.

lated by [60]

$$I_{\sigma}(V_b) = \frac{e}{h} \int_{-\infty}^{+\infty} T^{\sigma}(E, V_b) [f_d(E - \mu_d) - f_s(E - \mu_s)] dE, \quad (10)$$

where  $\sigma$ ,  $e$ ,  $h$ ,  $T^{\sigma}$ ,  $V_b$ ,  $f_{s/d}$ , and  $\mu_{s/d}$  are the spin state (spin up  $\uparrow$ , spin down  $\downarrow$ ), electron charge, Planck constant, spin-dependent transmission coefficient, bias voltage between the source and drain, the Fermi-Dirac distribution function  $f_{s/d} = \{1 + \exp[(E - \mu_{s/d})/k_B T_{s/d}]\}^{-1}$  of electrodes, and the chemical potential of the source/drain, respectively. The cur-

rent from the drain to the source is defined as a positive one; otherwise, it is called the negative current.

The calculated spin-dependent *I*-*V* curve is shown in Fig. 5(b). Clearly, the current is negligibly small under positive bias, while under reverse bias, the current for both spin states shows a nearly linear increase with increasing bias voltage. Therefore, this device demonstrates a significant unidirectional conduction, namely, a noticeable rectification effect. Additionally, the transport in the spin-up state is significantly superior to that in the spin-down state, indicating a spin-polarization effect. To quantitatively describe this characteristic, we calculate the spin-polarization ratio, defined as  $PR = (I_{\uparrow} - I_{\downarrow})/(I_{\uparrow} + I_{\downarrow})$ . The calculated results are shown



on the right axis of Fig. 5(b). At  $V_b = -0.3$  V, the spin polarization reaches 98.2%, and in the bias region from  $V_b = -0.3$  to 0.8 V, the spin polarization is very close to 100%, indicating that the spin-down transport in  $pn$  junction is almost blocked completely in such a bias region. However, in the bias region from  $V_b = -0.8$  to  $-0.3$  V, the spin-down state becomes conductive, significantly weakening the spin-polarization effect. To quantitatively describe the unidirectional conduction of the device, we calculate the rectification ratio defined as  $RR = |I(-V_b)/I(V_b)|$ , as shown in Fig. 5(c). Clearly, in the low-bias range (from  $V_b = 0,0$  to  $-0.3$  V), the rectification ratio in the spin-up state is higher than that in the spin-down state, while in the high-bias range (from  $V_b = -0.4$  to  $-0.8$  V), the situation is reversed. The rectification ratio in the spin-down state reaches its maximum ( $10^9$ ) at  $V_b = -0.5$  V.

To explain the spin transport property, the spin-resolved transmission spectra are presented in Figs. 5(d)–5(i) (left panel) at bias voltages  $V_b = 0.0$  V and  $\pm 0.8$  V, respectively. Compared to the transmission spectra at zero bias, at a negative bias of  $V_b = -0.8$  V, significant transmission peaks appear within the bias window (BW) for both the spin-up and spin-down states [see Figs. 5(f) and 5(g) in the left panel]. According to Eq. (10), the transport current is equal to the integral of the transmission coefficient within the BW. Therefore, under this negative bias, tunneling transport channels are opened for both spin states, resulting in larger currents for them. However, the transmission for the spin-up state is distributed inside the entire BW, while that for the spin-down state only occurs in a partial energy range of the BW. As a result, the current of the spin-up state is greater than that of the spin-down state, consistently with the  $I$ - $V$  characteristic, as mentioned above. While at  $V_b = 0.8$  V, transmission coefficients inside the BW for both spin states are zero, indicating a complete suppression of the transport channels, and therefore, no current is generated.

To provide a more intuitive identification for excellent rectification and spin-polarization effects of the device, we present the bias-dependent spin-resolved transmission spectra in Figs. 5(j) and 5(k). Under positive bias, no transmission arises inside the BW for both spin channels. However, under negative bias, the situation is significantly different; a larger transmission appears inside the BW, and the transmission intensity increases with increasing negative-bias magnitude. Furthermore, Figs. 5(j) and 5(k) reveal that for both spin states, the transmission only occurs within the BW, but the transmission for the spin-up state holds a broader distribution and higher intensity. This suggests that the total current in the BW is primarily contributed by the spin-up state. Figure 5(l) presents the differential conductance ( $dI/dV$ ) density curve. Similarly to the spin-resolved current, significant spin-polarization behavior in the differential conductance density can also be detected, particularly obviously in the bias range from 0.0 to  $-0.25$  V. Meanwhile, we can see that the spin-up current is changed more quickly with bias than the spin-down current. At  $V_b = -0.8$  V, the differential conductance density for total current reaches 2.91 S/mm.

To gain a deeper insight into the physical mechanisms for the bias-dependent spin-resolved transmission coefficient as well as spin-polarization and rectifying effects, Figs. 5(d)–5(i) (right panel) present the projected local density of states (PL-

DOS), where the white region represents the blockage zone (band gap between CBM and VBM) for electronic transport. At  $V_b = 0.0$  V, for the two spin states, typical energy band alignment for  $pn$  junction can clearly be seen [the right panels in Figs. 5(d) and 5(e)]. As stated before, the left (right) area is exerted with the  $p$ ( $n$ )-type doping; thus, carrier diffusion takes place across the midlined interface due to their carrier concentration difference, leading to the formation of a space-charge layer, and in turn a built-in electric field is established from the  $n$ -doped region pointing to the  $p$ -doped region, which hinders the diffusion of carriers further. Finally, the diffusion and drift of carriers reach an equilibrium, and a typical  $pn$  junction is formed. While under negative bias, for example, at  $V_b = -0.8$  V [see the right panels in Figs. 5(f) and 5(g)], the bias effect causes the CBM and VBM of the  $n$ ( $p$ )-type doping area shift downwards (upwards), resulting in a higher electronic states entering into the BW on both areas. Specifically, from the perspective of band alignment, the VBM of the  $p$ -type doping area inside the BW is higher than the CBM of the  $n$ -type doping area, causing electron tunneling from the valence band of the  $p$ -type doping area, including the source electrode, to the conduction band of the  $n$ -type doping area, including the drain electrode. This leads to higher electronic transmission coefficients and larger tunneling currents, particularly evident for the spin-up states due to its thinner barrier width in the central scattering region. With positive bias, for example, at  $V_b = 0.8$  V [see the right panels in Figs. 5(h) and 5(i)], the situation is reversed; the bias effect causes the CBM and VBM of the  $n$ ( $p$ )-type doping region to shift upwards (downwards) and the electronic states in the BW are removed. Correspondingly, the tunneling channel for electrons is closed completely, resulting in zero transmission and thus zero current occurring at this bias. In short, the strong rectification effect observed in this diode is attributed to the prominent modulation of electronic state by bias polarity. The generation of spin-filtering effect is intimately related to the inherent spin-dependent band gap of ML-MBTS; the spin-up channel with a smaller band gap is more sensitive to bias.

Furthermore, the  $I$ - $V$  characteristics of the device can also be described by the following equation [61]:

$$I = I_0 e^{qV_b/nk_B T} (1 - e^{-qV_b/k_B T}), \quad (11)$$

where  $I_0$ ,  $q$ ,  $V_b$ ,  $n$ , and  $T$  represent the saturation current, elementary charge, bias voltage, ideality factor, and temperature, respectively. In general, the value of  $n$  can be used to assess the performance of the device. When  $n = 1$ , it means that there are no defects in device, and the transport current is primarily governed by diffusion. If  $n = 2$ , the transport current is mainly constituted with the recombination current due to excessive defect states existing in the device. The practical  $pn$  junction always contains recombination centers; the value of  $n$  typically falls between 1 and 2. In our case, the ideality factor  $n$  can be extracted from the slope of the logarithmic plot of  $I/(1 - e^{-qV_b/k_B T})$  associated with  $V_b$ , as shown in Fig. 5(m). The ideality factor increases gradually with temperature. Under room-temperature conditions, the derived ideality factor for the  $A$ -type diode is 1.18, indicating that it is close an ideal behavior. Even at a high temperature of 600 K, the ideality factor remains at 1.42 [see Fig. 5(n)]; that is, the device performance is affected less by temperature and

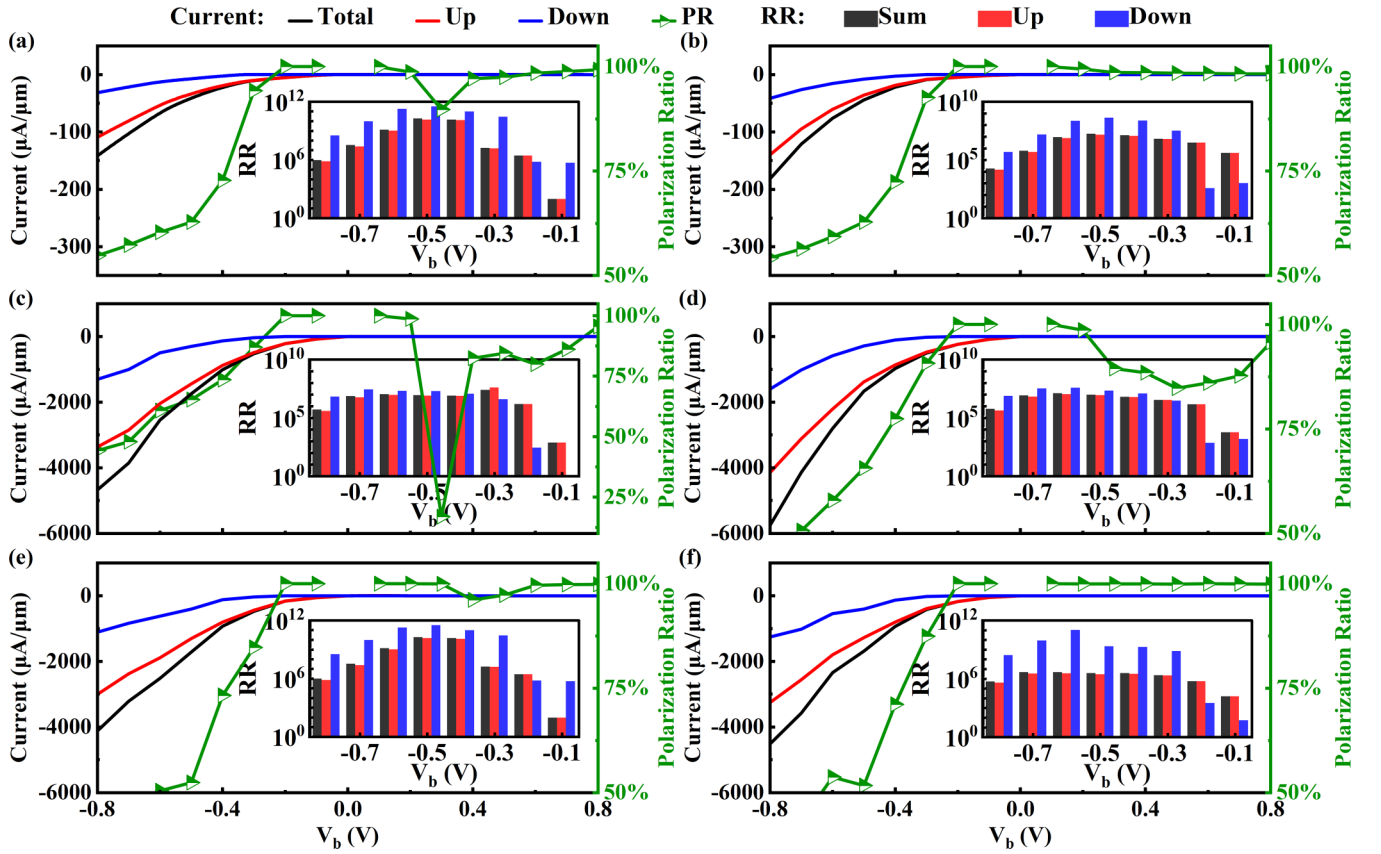


FIG. 6.  $I$ - $V$  curve, spin-polarization ratio, and rectification ratio (inset) for A-, Z-type  $pin$ -junction field-effect transistor at several typical gate voltages: (a), (b)  $V_g = 0.0$  V; (c), (d)  $V_g = 10$  V; and (e), (f)  $V_g = -10$  V.

can stably operate at room temperature, while for the Z-type diode, with the transport direction along the zigzag direction of ML-MBTS, its rectification and spin-filtering behaviors as well as the physical mechanisms are basically similar to the A-type diode [see Fig. S8 [38] for more details]. In short, the ML-MBTS  $pn$ -junction diodes, regardless of A type or Z type, all exhibit outstanding spin-filtering and rectification features, promising a great potential for applications in the sub-3 nm spin-filtering devices and rectifiers.

## 2. Sub-3 nm field-effect transistor and phototransistor

Similarly to the above suggested ML-MBTS  $pn$ -junction diode, the ML-MBTS  $pin$ -junction field-effect transistor (FET) is constructed by  $n/p$ -type doping at source/drain electrodes, but a sub-3 nm channel based on intrinsic ML-MBTS is used for carried transport. The doping concentration for electrodes is  $6 \times 10^{13}$ ,  $\text{cm}^{-2}$ . The top and bottom gates are located above and below the central scattering region, respectively, with a relative dielectric constant of 7.8 and a thickness of 15 Å. The effective oxide thickness is 7.5 Å. The spin-resolved current in such a device can be calculated by

$$I_{\sigma}(V_b, V_g) = \frac{e}{h} \int_{-\infty}^{+\infty} T^{\sigma}(E, V_b, V_g) \times [f_d(E - \mu_d) - f_s(E - \mu_s)] dE \quad (12)$$

where  $V_g$  is the gate voltage. Here, we consider two types of  $pin$ -junction FETs, A type and Z type, with the electronic transport direction occurring in armchair and zigzag direction, respectively. Figures 6(a) and 6(b) shows the  $I$ - $V$  curve, polarization ratio, and rectification ratio for A/Z-type  $pin$ -junction FETs in the case of  $V_g = 0.0$  V. Compared to the  $pn$  junction, the current density in such a device is significantly suppressed due to the intrinsic semiconducting MBTS acting as device channel, as mentioned above. The current density in the spin-up state is higher than that in the spin-down state, and the device still exhibits spin filtering and rectification effects, similarly to the  $pn$  junction. In particular, the maximum rectification ratio for the A-type  $pin$  junction in the spin-down state is enhanced to  $10^{11}$ , which is two orders of magnitude higher than that of the  $pn$  junction in the spin-down state, indicating its advantages in designing high-performance rectifiers.

To reveal the field-effect behavior for the  $pin$  junction, we present the  $I$ - $V$  curves, polarization ratio, and rectification ratio for the device at gate voltages of  $V_g = 10$  and  $-10$  V, respectively, in Figs. 6(c)–6(f). Clearly, the device exhibits a substantial field-effect behavior, with a significantly enhanced current density under gate voltage, regardless of it is positive or negative. Meanwhile, we find that the Z-type  $pin$  junction displays a higher polarization ratio than the A-type  $pin$  junction. Their polarization ratio is higher under positive-bias voltage, but decreases almost linearly with increasing negative-bias voltage. Furthermore, their polarization ratio is

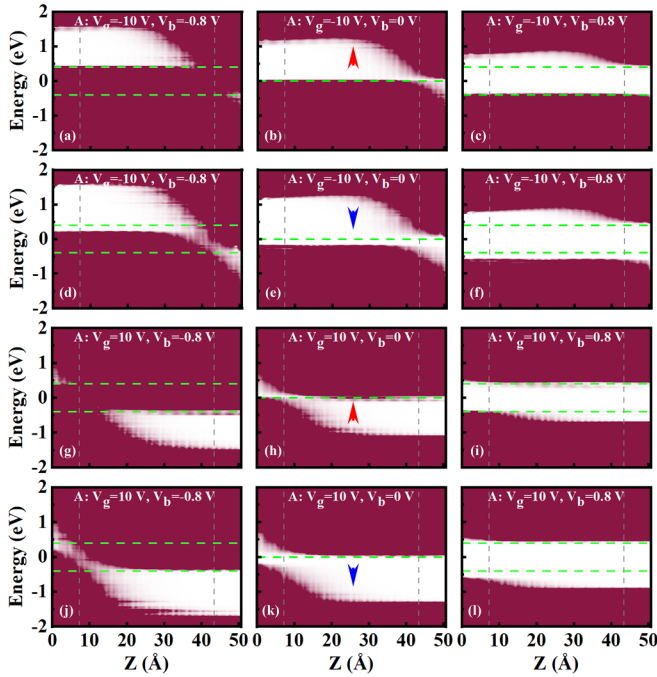


FIG. 7. PLDOS for A-type *pin* junction. Gate voltage is fixed as  $V_g = -10$  V, and bias voltages are taken as (a), (d)  $V_b = -0.8$  V; (b), (e)  $V_b = 0.0$  V; and (c), (f)  $V_b = 0.8$  V for spin-up/spin-down states. Fixing  $V_g = 10$  V, and bias voltages are set as (g), (j)  $V_b = -0.8$  V; (h), (k)  $V_b = 0.0$  V; and (i), (l)  $V_b = 0.8$  V for spin-up/spin-down states.

higher under negative gate voltages. It is worth noting that within the range from  $V_b = -0.2$  to  $0.8$  V, the Z-type *pin* junction achieves 100% spin polarization under a gate voltage of  $-10$  V [Fig. 6(f)]. These results indicate the possible applications for the ML-MBTS *pin*-junction spin field-effect transistors acting as spin-filtering devices.

The field-effect behavior as well as the spin-filtering and rectification effects for *pin*-junction devices can also be understood by the spin-resolved and bias- and gate-voltage-dependent PLDOS, as shown in Fig. 7 (for A-type *pin* junction) and Figs. S9 and S10 [38] (for both A- and Z-type *pin* junctions). In comparison with the PLDOS in the spin-down state, we can see that the spin-up state always exhibits a smaller band gap for both Z- and A-type *pin* junctions, regardless of gate- and bias voltages, making it more favorable for electronic tunneling. For the A-type *pin* junction (see Fig. 7), when  $V_g = \pm 10$  V and  $V_b = 0.0$  V, it is observed that the band bending is strengthened further and the band-gap region (blockage zone for electronic tunneling) is varied significantly for both spin states [see Figs. 7(b), 7(e), 7(h), and 7(k)] as compared to the case  $V_g = V_b = 0.0$  V (see Fig. S9 [38]), showing the evident field-effect feature, which is also observed at other  $V_b$  by comparing the case with and without  $V_g$ . Taking  $V_g = \pm 10$  V and  $V_b = -0.8$  V [see Figs. 7(a) and 7(g)], we find that the spin-up electronic states completely occupy the entire BW, leading to a larger current due to strong thermionic emission [62], while for spin-down electronic states [see Figs. 7(d) and 7(j)], the partial band gap of ML-MBTS falls in the BW, leading to a smaller current compared to the case of the spin-up state. Therefore, the spin-

polarization effect emerges. When  $V_g = \pm 10$  V and  $V_b = 0.8$  V, the electronic states for both spin orientations are completely removed from the BW; namely, the BW is included in the ML-MBTS band gap entirely, making electron tunneling prohibited. Therefore, the A-type *pin* junction features a significant rectifying effect; that is, the bias-polarity-dependent highly asymmetric channel barriers in device induce an excellent rectification, while for Z-type *pin* junction, the physical mechanism of its spin transport is essentially similar to the A-type [see Figs. S9 and S10 [38] for details].

Furthermore, we construct two other types of ML-MBTS-based FETs, *nin* and the *pip* junctions, similarly to *pin* junction as presented above. The difference is only that both source and drain electrodes are doped with the same type, *p* type or *n* type. The calculated *I-V* characteristics for *nin* and the *pip* junctions at  $V_g = 0.0$  V, as displayed in Fig. 8. It shows that both types of FETs exhibit negative differential resistance (NDR) phenomenon in the spin-up state [63] and a significantly high spin-filtering effect. The NDR effect is more pronounced in the *nin* junction, while the *pip* junction achieves a perfect spin filtering, with 100% polarization ratio in whole bias region by spin-down current suppressed completely, suggesting that ML-MBTS-based *pip* junction is an ideal candidate for developing the future spin field-effect transistors as a perfect spin filter.

Finally, we examine the potential application of ML-MBTS in the field of spin optoelectronic devices for six types of model structure: A/Z-type *pin* junction, *nin* junction, and *pip* junction, as described above. The calculation of photocurrent is considered by linearly polarized incident light with photon energy ranging from 0.0 to 5.0 eV. When a photon with frequency  $\omega$  is absorbed by the electrodes of the ML-MBTS phototransistor, the generated photocurrent can be calculated by [64,65]

$$I_\alpha = \frac{e}{h} \int_{-\infty}^{+\infty} \sum_{\beta=d,s} [1 - f_\alpha(E)] f_\beta(E - \hbar\omega) T_{\alpha,\beta}^-(E) - f_\alpha(E) \times [1 - f_\beta(E + \hbar\omega)] T_{\alpha,\beta}^+(E) dE, \quad (13)$$

where  $\alpha = d/s$ , and the total photocurrent  $I_{ph} = I_d - I_s$ . Under zero bias (without power), the calculated results are plotted in Fig. 9. Based on the AM1.5 standard, the A-type *pin*-junction phototransistor exhibits significant photocurrent peaks in the yellow- and blue-light regions, with the yellow/blue-light photocurrent mainly contributed by spin-up/spin-down state. This indicates that for designing the related spin photodetectors, the different spin-dependent light responses can be utilized to distinguish colors of light [see Fig. 9(a)]. The Z-type *pin*-junction phototransistor exhibits an excellent light response to yellow light, mainly contributed by spin-up states, with a photocurrent as high as  $278.76 \mu\text{A}/\text{mm}^2$ , significantly higher than silicon solar-cell devices [64] and  $\text{MoSi}_2\text{P}_4$  *pin*-junction phototransistors [66] [see Fig. 9(d)]. The A-type *nin*-junction phototransistor generates a prominent negative photocurrent peak in the ultraviolet light region, almost entirely contributed by spin-up states, indicating a reversed directional photocurrent produced at the source electrode leaks to the drain electrode [see Fig. 9(b)]. The Z-type *nin*-junction phototransistor exhibits positive and negative photocurrent

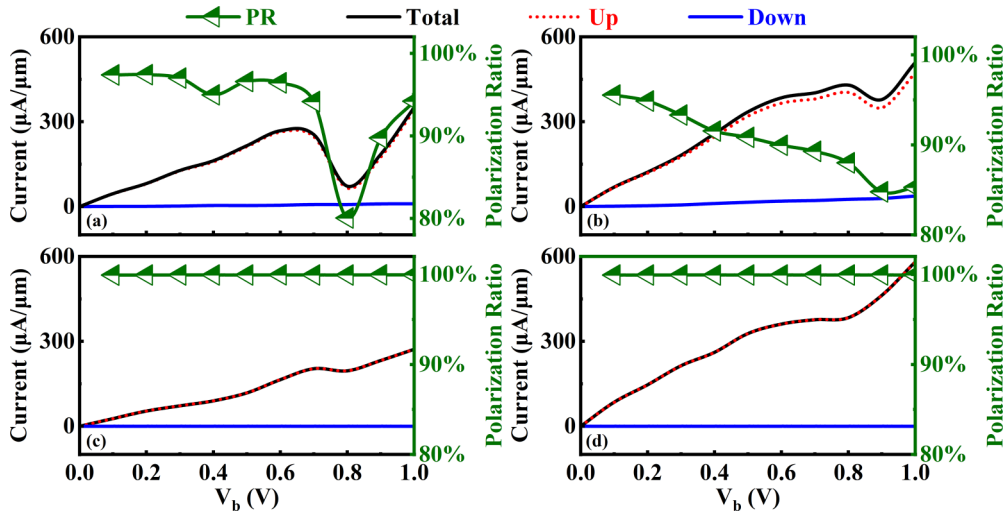


FIG. 8.  $I$ - $V$  curve and spin-polarization ratio at  $V_g = 0.0$  V for (a) A-type *nin* junction, (b) Z-type *nin* junction, (c) A-type *pip* junction, and (d) Z-type *pip* junction.

peaks in the green- and blue-light regions, respectively; both of them are primarily contributed by the spin-up state, which is associated with its smaller band gap, resulting in a higher photon absorption efficiency upon *n*-type doping in electrodes [see Fig. 9(e)]. The A-type *pip*-junction phototransistor possesses a photocurrent peak contributed mainly by the spin-up state in the orange-/purple-light regions and produces photocurrents with almost equal magnitude but in opposite direction in the blue-light region [see Fig. 9(c)]. The Z-type *pip*-junction phototransistor exhibits a large spin-up state photocurrent in the blue- and ultraviolet-light regions [see Fig. 9(f)]. Comparing these results, it can be concluded that ML-MBTS *pin*-junction phototransistors hold a superior performance and are ideal candidate for designing solar cells and optoelectronic devices.

#### IV. CONCLUSIONS

In summary, we have systematically investigated the structural stability, magnetoelectronics, and mechanical, optical,

and transport properties of ML-MBTS by using the density-functional theory combined with the nonequilibrium Green function. The energetic, dynamic, thermal, and mechanic stability of ML-MBTS has been highly identified by the calculated cohesive energy, phonon spectrum, molecular dynamics simulation, and elastic constant relation, implying that ML-MBTS possibly exists in experiment. The ML-MBTS is a HSC in the FM ground state, stemming from GKA superexchange magnetic interaction. The out-of-plane easy axis of magnetization, holding a higher magnetic anisotropy energy, enhances the stability of magnetic ordering. The calculated Curie temperature for ML-MBTS is up to 54.3 K, which is higher than the part of currently already-fabricated magnetic materials. It also holds outstanding mechanical and optical properties; for example, the relatively lower Young's modulus and anisotropic Poisson's ratio for ML-MBTS suggest its potential applications in flexible nanoelectronic strain sensors, and the high optical absorption characteristics in the ultraviolet range suggests its potential in developing photovoltaic devices within the

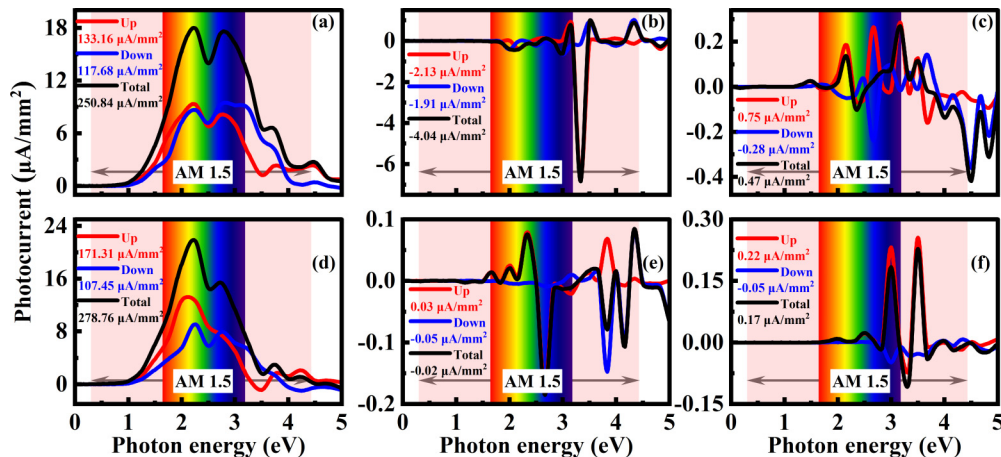


FIG. 9. Photocurrent for A-, Z-type spin phototransistors constructed with (a), (d) *pin* junction; (b), (e) *nin* junction; and (c), (f) *pip* junction under zero bias (without power).

AM1.5 standard. And also, it has a high carrier mobility,  $\sim 10^5 \text{ cm}^2 \text{ V}^{-1} \text{ s}^{-1}$ .

Besides, we have designed multiple kinds of sub-3 nm functional device prototypes. It has been found that such devices possess excellent transport behaviors. For example, the *pn*-junction diode exhibits a high spin filtering and strong rectification effect, with a rectification ratio up to  $10^9$ . The rectification effect for *A*-type *pin*-junction field-effect transistor is more advantageous, with rectification ratio reaching  $10^{11}$ , and the bias-polarity-dependent highly asymmetric channel barriers in device is responsible to such a excellent rectification. The *nin* junction and *pip* junction field-effect transistors manifest an intriguing NDR phenomenon and spin-filtering effect. Particularly, the *pip*-junction field-effect transistor achieves 100% spin filtering in the region of

whole calculated bias voltage. Furthermore, the *pin*-junction phototransistor exhibits excellent optical response and can distinguish colors based on the magnitude of spin-up and spin-down photocurrents. These findings indicate that the suggested ML-MBTS can emerge as a promising material for developing nanoscale magnetic and optoelectronic devices.

## ACKNOWLEDGMENTS

This work is supported by the National Natural Science Foundation of China (Grant No. 61771076), the Hunan Provincial Natural Science Foundation of China (Grant No. 2021JJ30733), and Postgraduate Scientific Research Innovation Project of Hunan Province, China (Grant No. CX20220957).

- 
- [1] M. Hossain, B. Qin, B. Li, and X. D. Duan, Synthesis, characterization, properties and applications of two-dimensional magnetic materials, *Nano Today* **42**, 101338 (2022).
- [2] W. J. Liu, H. X. Zhang, J. A. Shi, Z. C. Wang, C. Song, X. R. Wang, S. Y. Lu, X. J. Zhou, L. Gu, D. V. Louzguine-Luzgin, M. W. Chen, K. F. Yao, and N. Chen, A room-temperature magnetic semiconductor from a ferromagnetic metallic glass, *Nat. Commun.* **7**, 13497 (2016).
- [3] S. Kumari, D. K. Pradhan, N. R. Pradhan, and P. D. Rack, Recent developments on 2D magnetic materials: Challenges and opportunities, *Emerg. Mater.* **4**, 827 (2021).
- [4] Z. X. Shen, C. X. Su, and L. X. He, High-throughput computation and structure prototype analysis for two-dimensional ferromagnetic materials, *npj Comput. Mater.* **8**, 132 (2022).
- [5] Z. Wang, M. Gibertini, D. Dumcenco, T. S. Taniguchi, K. J. Watanabe, E. Giannini, and A. F. Morpurgo, Determining the phase diagram of atomically thin layered antiferromagnet  $\text{CrCl}_3$ , *Nat. Nanotechnol.* **14**, 1116 (2019).
- [6] V. Ostwal, T. T. Shen, and J. Appenzeller, Efficient spin-orbit torque switching of the semiconducting van der Waals ferromagnet  $\text{Cr}_2\text{Ge}_2\text{Te}_6$ , *Adv. Mater.* **32**, 1906021 (2020).
- [7] K. S. Novoselov, A. K. Geim, S. V. Morozov, D. Jiang, Y. Zhang, S. V. Dubonos, I. V. Grigorieva, and A. A. Firsov, Electric field effect in atomically thin carbon films, *Science* **306**, 666 (2004).
- [8] H. Pan, L. Tang, and K. Chen, Quantum mechanical modeling of magnon-phonon scattering heat transport across three-dimensional ferromagnetic/nonmagnetic interfaces, *Phys. Rev. B* **105**, 064401 (2022).
- [9] Z. Ding, Y. Zeng, H. Pan, N. Luo, J. Zeng, L. Tang, and K. Chen, Edge states of topological acoustic phonons in graphene zigzag nanoribbons, *Phys. Rev. B* **106**, L121401 (2022).
- [10] R. He, D. Wang, N. Luo, J. Zeng, K. Chen, and L. Tang, Nonrelativistic spin-momentum coupling in antiferromagnetic twisted bilayers, *Phys. Rev. Lett.* **130**, 046401 (2023).
- [11] H. Pan, Z. Ding, B. Zeng, N. Luo, J. Zeng, L. Tang, and K. Chen, Ab initio Boltzmann approach to coupled magnon-phonon thermal transport in ferromagnetic crystals, *Phys. Rev. B* **107**, 104303 (2023).
- [12] C. Gong, L. Li, Z. L. Li, H. W. Ji, A. Stern, Y. Xia, T. Cao, W. Bao, C. Z. Wang, Y. Wang, Z. Q. Qiu, R. J. Cava, S. G. Louie, J. Xia, and X. Zhang, Discovery of intrinsic ferromagnetism in two-dimensional van der Waals crystals, *Nature (London)* **546**, 265 (2017).
- [13] B. Huang, G. Clark, E. N. Moratalla, D. R. Klein, R. Cheng, K. L. Seyler, D. Zhong, E. Schmidgall, M. A. McGuire, D. H. Cobden, W. Yao, D. Xiao, P. J. Herrero, and X. D. Xu, Layer-dependent ferromagnetism in a van der Waals crystal down to the monolayer limit, *Nature (London)* **546**, 270 (2017).
- [14] Y. J. Deng, Y. J. Yu, Y. C. Song, J. Z. Zhang, N. Z. Wang, Z. Y. Sun, Y. F. Yi, Y. Z. Wu, S. W. Wu, J. Y. Zhu, J. Wang, X. H. Chen, and Y. B. Zhang, Gate-tunable room-temperature ferromagnetism in two-dimensional  $\text{Fe}_3\text{GeTe}_2$ , *Nature (London)* **563**, 94 (2018).
- [15] M. Bonilla, S. Kolekar, Y. J. Ma, H. C. Diaz, V. Kalappattil, R. Das, T. Eggers, H. R. Gutierrez, M. H. Phan, and M. Batzill, Strong room-temperature ferromagnetism in  $\text{VSe}_2$  monolayers on van der Waals substrates, *Nat. Nanotechnol.* **13**, 289 (2018).
- [16] Y. Gong, J. W. Guo, J. H. Li, K. J. Zhu, M. H. Liao, X. Z. Liu, Q. H. Zhang, L. Gu, L. Tang, and X. Feng, Experimental realization of an intrinsic magnetic topological insulator, *Chin. Phys. Lett.* **36**, 076801 (2019).
- [17] M. M. Otrokov, I. I. Klimovskikh, H. Bentmann, D. Estyunin, A. Zeugner, Z. S. Aliev, S. Gaß, A. U. B. Wolter, A. V. Koroleva, A. M. Shikin, M. Blanco-Rey, M. Hoffmann, I. P. Rusinov, A. Yu. Vyazovskaya, S. V. Ereemeev, Yu. M. Koroteev, V. M. Kuznetsov, F. Freyse, J. Sánchez-Barriga, I. R. Amiraslanov, M. B. Babanly, N. T. Mamedov, N. A. Abdullayev, V. N. Zverev, A. Alfonsov, V. Kataev, B. Büchner, E. F. Schwier, S. Kumar, A. Kimura, L. Petaccia, G. Di Santo, R. C. Vidal, S. Schatz, K. Kißner, M. Ünzelmann, C. H. Min, Simon Moser, T. R. F. Peixoto, F. Reinert, A. Ernst, P. M. Echenique, A. Isaeva, and E. V. Chulkov, Prediction and observation of an antiferromagnetic topological insulator, *Nature (London)* **576**, 416 (2019).
- [18] D. Q. Zhang, M. J. Shi, T. H. Zhu, D. Y. Xing, H. J. Zhang, and J. Wang, Topological axion states in the magnetic insulator  $\text{MnBi}_2\text{Te}_4$  with the quantized magnetoelectric effect, *Phys. Rev. Lett.* **122**, 206401 (2019).
- [19] J. H. Li, Y. Li, S. Q. Du, Z. Wang, B. L. Gu, S. C. Zhang, K. He, W. H. Duan, and Y. Xu, Intrinsic magnetic topological

- insulators in van der Waals layered  $\text{MnBi}_2\text{Te}_4$ -family materials, *Sci. Adv.* **5**, eaaw5685 (2019).
- [20] M. M. Otrokov, I. P. Rusinov, M. Blanco-Rey, M. Hoffmann, A. Yu. Vyazovskaya, S. V. Eremin, A. Ernst, P. M. Echenique, A. Arnau, and E. V. Chulkov, Unique thickness-dependent properties of the van der Waals interlayer antiferromagnet  $\text{MnBi}_2\text{Te}_4$  films, *Phys. Rev. Lett.* **122**, 107202 (2019).
- [21] J. H. Li, C. Wang, Z. Zhang, B. L. Gu, W. H. Duan, and Y. Xu, Magnetically controllable topological quantum phase transitions in the antiferromagnetic topological insulator  $\text{MnBi}_2\text{Te}_4$ , *Phys. Rev. B* **100**, 121103(R) (2019).
- [22] B. Li, J. Q. Yan, D. M. Pajerowski, E. Gordon, A. M. Nedić, Y. Sizyuk, L. Q. Ke, P. P. Orth, D. Vaknin, and R. J. McQueeney, Competing magnetic interactions in the antiferromagnetic topological insulator  $\text{MnBi}_2\text{Te}_4$ , *Phys. Rev. Lett.* **124**, 167204 (2020).
- [23] L. Y. Mei, J. Xiao, and K. Chang, Topological magnon modes in patterned ferrimagnetic insulator thin films, *Nano Lett.* **18**, 3032 (2018).
- [24] C. Liu, Y. C. Wang, H. Li, Y. Wu, Y. X. Li, J. H. Li, K. He, Y. Xu, J. S. Zhang, and Y. Y. Wang, Robust axion insulator and Chern insulator phases in a two-dimensional antiferromagnetic topological insulator, *Nat. Mater.* **19**, 522 (2020).
- [25] Y. J. Deng, Y. J. Yu, M. Z. Shi, Z. X. Guo, Z. H. Xu, J. Wang, X. H. Chen, and Y. B. Zhang, Quantum anomalous Hall effect in intrinsic magnetic topological insulator  $\text{MnBi}_2\text{Te}_4$ , *Science* **367**, 895 (2020).
- [26] H. L. Li, C. Z. Chen, H. Jiang, and X. C. Xie, Coexistence of quantum Hall and quantum anomalous Hall phases in disordered  $\text{MnBi}_2\text{Te}_4$ , *Phys. Rev. Lett.* **127**, 236402 (2021).
- [27] Y. P. An, K. Wang, S. J. Gong, Y. S. Hou, C. L. Ma, M. F. Zhu, C. X. Zhao, T. X. Wang, S. H. Ma, H. Y. Wang, R. Q. Wu, and W. M. Liu, Nanodevices engineering and spin transport properties of  $\text{MnBi}_2\text{Te}_4$  monolayer, *npj Comput. Mater.* **7**, 45 (2021).
- [28] Z. Yan, X. Jia, X. W. Shi, X. L. Dong, and X. H. Xu, Barrier-dependent electronic transport properties in two-dimensional  $\text{MnBi}_2\text{Te}_4$ -based van der Waals magnetic tunnel junctions, *Appl. Phys. Lett.* **118**, 223503 (2021).
- [29] G. H. Zhan, Z. L. Yang, K. Luo, D. Zhang, W. K. Lou, J. T. Liu, Z. H. Wu, and K. Chang, Spin-dependent tunneling in 2D  $\text{MnBi}_2\text{Te}_4$ -based magnetic tunnel junctions, *MRS Bull.* **47**, 1177 (2022).
- [30] X. Chen and Z. Z. Lin, 2D spin transport through graphene- $\text{MnBi}_2\text{Te}_4$  heterojunction, *Nanotechnology* **33**, 325201 (2022).
- [31] Q. R. Cui, Y. M. Zhu, J. H. Liang, P. Cui, and H. X. Yang, Antiferromagnetic topological magnetism in synthetic van der Waals antiferromagnets, *Phys. Rev. B* **107**, 064422 (2023).
- [32] J. Y. You, X. J. Dong, B. Gu, and G. Su, Electric field induced topological phase transition and large enhancements of spin-orbit coupling and Curie temperature in two-dimensional ferromagnetic semiconductors, *Phys. Rev. B* **103**, 104403 (2021).
- [33] S. Smidstrup, T. Markussen, P. Vancaeyveld, J. Wellendorff, J. Schneider, T. Gunst, B. Verstichel, D. Stradi, P. A. Khomyakov, U. G. Vej-Hansen, M. E. Lee, S. T. Chill, F. Rasmussen, G. Penazzi, F. Corsetti, A. Ojanperä, K. Jensen, M. Palsgaard, U. Martinez, A. Blom, M. Brandbyge, and K. Stokbro, QuantumATK: An integrated platform of electronic and atomic-scale modelling tools, *J. Phys.: Condens. Matter* **32**, 015901 (2019).
- [34] J. P. Perdew, K. Burke, and M. Ernzerhof, Generalized gradient approximation made simple, *Phys. Rev. Lett.* **77**, 3865 (1996).
- [35] A. Rohrbach, J. Hafner, and G. Kresse, Molecular adsorption on the surface of strongly correlated transition-metal oxides: A case study for CO/NiO(100), *Phys. Rev. B* **69**, 075413 (2004).
- [36] J. Heyd, G. E. Scuseria, and M. Ernzerhof, Hybrid functionals based on a screened Coulomb potential, *J. Chem. Phys.* **118**, 8207 (2003).
- [37] G. J. Martyna, M. L. Klein, and M. Tuckerman, Nosé-Hoover chains: The canonical ensemble via continuous dynamics, *J. Chem. Phys.* **97**, 2635 (1992).
- [38] See Supplemental Material at <http://link.aps.org/supplemental/10.1103/PhysRevB.108.184413> for additional figures in support of the data analysis.
- [39] J. Kanamori, Crystal distortion in magnetic compounds, *J. Appl. Phys.* **31**, S14 (1960).
- [40] J. B. Goodenough, Theory of the role of covalence in the Perovskite-Type Manganites  $[\text{La}, \text{M}(\text{II})]\text{MnO}_3$ , *Phys. Rev.* **100**, 564 (1955).
- [41] P. W. Anderson, New approach to the theory of superexchange interactions, *Phys. Rev.* **115**, 2 (1959).
- [42] M. Gibertini, M. Koperski, A. F. Morpurgo, and K. S. Novoselov, Magnetic 2D materials and heterostructures, *Nature Nanotechnol.* **14**, 408 (2019).
- [43] A. I. Liechtenstein, M. I. Katsnelson, V. P. Antropov, and V. A. Gubanov, Local spin density functional approach to the theory of exchange interactions in ferromagnetic metals and alloys, *J. Magn. Magn. Mater.* **67**, 65 (1987).
- [44] P. Bruno, Exchange interaction parameters and adiabatic spin-wave spectra of ferromagnets: A “renormalized magnetic force theorem,” *Phys. Rev. Lett.* **90**, 087205 (2003).
- [45] A. Terasawa, M. Matsumoto, T. Ozaki, and Y. Gohda, Efficient algorithm based on Liechtenstein method for computing exchange coupling constants using localized basis set, *J. Phys. Soc. Jpn.* **88**, 114706 (2019).
- [46] D. Vaknin, D. M. Pajerowski, D. L. Schlagel, K. W. Dennis, and R. J. McQueeney, Two-dimensional ordering and collective magnetic excitations in the dilute ferromagnetic topological insulator  $(\text{Bi}_{0.95}\text{Mn}_{0.05})_2\text{Te}_3$ , *Phys. Rev. B* **99**, 220404(R) (2019).
- [47] H. S. Zhang, J. J. Zhang, Y. L. Zhang, W. J. Yang, Y. Y. Wang, X. H. Xu, and F. Liu, A generic dual d-band model for interlayer ferromagnetic coupling in a transition-metal doped  $\text{MnBi}_2\text{Te}_4$  family of materials, *Nanoscale* **14**, 13689 (2022).
- [48] X. X. Li and J. L. Yang, First-principles design of spintronics materials, *Nat. Sci. Rev.* **3**, 365 (2016).
- [49] J. Przystawa and W. Suski, Magnetic ordering in uranium compounds with crystal structures of anti- $\text{Cu}_2\text{Sb}$  and  $\text{PbFCl}$  types. molecular field approximation, *Phys. Status Solidi* **20**, 451 (1967).
- [50] J. Bardeen and W. Shockley, Deformation potentials and mobilities in non-polar crystals, *Phys. Rev.* **80**, 72 (1950).
- [51] Y. Q. Cai, G. Zhang, and Y. W. Zhang, Polarity-reversed robust carrier mobility in monolayer  $\text{MoS}_2$  nanoribbons, *J. Am. Chem. Soc.* **136**, 6269 (2014).
- [52] Z. G. Shao, X. S. Ye, L. Yang, and C. L. Wang, First-principles calculation of intrinsic carrier mobility of silicene, *J. Appl. Phys.* **114**, 093712 (2013).

- [53] R. C. Andrew, R. E. Mapasha, A. M. Ukpong, and N. Chetty, Erratum: Mechanical properties of graphene and boronitrene, *Phys. Rev. B* **85**, 125428 (2012); **100** 209901(E) (2019).
- [54] E. Cadelano, P. L. Palla, S. Giordano, and L. Colombo, Elastic properties of hydrogenated graphene, *Phys. Rev. B* **82**, 235414 (2010).
- [55] P. Nandi, A. Rawat, R. Ahammed, N. Jena, and A. D. Sarkar, Group-IV(A) Janus dichalcogenide monolayers and their interfaces straddle gigantic shear and in-plane piezoelectricity, *Nanoscale* **13**, 5460 (2021).
- [56] J. Toll, Causality and the dispersion relation: Logical foundations, *Phys. Rev.* **104**, 1760 (1956).
- [57] H. Y. Chen, K. W. Liu, L. F. Hu, A. A. A. Ghamdi, and X. S. Fang, New concept ultraviolet photodetectors, *Mater. Today* **18**, 502 (2015).
- [58] ASTM G177-03(2012), Standard tables for reference solar spectral irradiances: direct normal and hemispherical on 37 tilted surface, ASTM International, West Conshohocken, PA, 2012, [www.astm.org](http://www.astm.org).
- [59] M. M. Dong, H. He, Y. Niu, C. K. Wang, and X. X. Fu, Prediction of semiconducting 2D nanofilms of Janus  $\text{WSi}_2\text{P}_2\text{As}_2$  for applications in sub-5 nm field-effect transistors, *ACS Appl. Nano Mater.* **6**, 1541 (2023).
- [60] J. P. Perdew and A. Zunger, Self-interaction correction to density-functional approximations for many-electron systems, *Phys. Rev. B* **23**, 5048 (1981).
- [61] D. Stradi, U. Martinez, A. Blom, M. Brandbyge, and K. Stokbro, General atomistic approach for modeling metal-semiconductor interfaces using density functional theory and nonequilibrium Green's function, *Phys. Rev. B* **93**, 155302 (2016).
- [62] Z. H. Li, J. N. Han, S. G. Cao, and Z. H. Zhang,  $\text{NbS}_2/\text{MoSi}_2\text{P}_4$  van der Waals heterojunction: Flexibly tunable electrical contact properties and potential applications for Schottky junction devices, *Appl. Surf. Sci.* **636**, 157766 (2023).
- [63] B. Q. Xu and Y. Dubi, Negative differential conductance in molecular junctions: An overview of experiment and theory, *J. Phys.: Condens. Matter* **27**, 263202 (2015).
- [64] M. Palsgaard, T. Markussen, T. Gunst, M. Brandbyge, and K. Stokbro, Efficient first-principles calculation of phonon-assisted photocurrent in large-scale solar-cell devices, *Phys. Rev. Appl.* **10**, 014026 (2018).
- [65] L. Zhang, K. Gong, J. Z. Chen, L. Liu, Y. Zhu, D. Xiao, and H. Guo, Generation and transport of valley-polarized current in transition-metal dichalcogenides, *Phys. Rev. B* **90**, 195428 (2014).
- [66] Y. F. Gao, J. B. Liao, H. Y. Wang, Y. Wu, Y. L. Li, K. Wang, C. L. Ma, S. J. Gong, T. X. Wang, X. Dong, Z. Y. Jiao, and Y. P. An, Electronic transport properties and nanodevice designs for monolayer  $\text{MoSi}_2\text{P}_4$ , *Phys. Rev. Appl.* **18**, 034033 (2022).